Optical and Quantum Electronics (2022) 54:766
https://doi.org/10.1007/s11082-022-04150-4

Consequence of Fibonacci quasiperiodic sequences in 1-D photonic crystal refractive index sensor for the blood plasma and cancer cells detections

Bipin K. Singh[1] · Priyanka S. Rajput[2] · Ashutosh K. Dikshit[3] · Praveen C. Pandey[4] · Vaishali Bambole[1]

Received: 30 December 2021 / Accepted: 26 August 2022 / Published online: 27 September 2022

Abstract
We present the consequences of different Fibonacci quasiperiodic sequences on the sensing performance of a one-dimensional (1D) photonic crystal (PC) based sensor to detect the blood plasma and cancer cells. We demonstrate that the sensitivity and figure of merit (FOM) of the sensor can be modulated, respectively, from 427.5 nm/RIU to 530 nm/RIU and from 162.5 RIU^{-1} to 2983.33 RIU^{-1} by utilizing the pertinent sensor structures with Fibonacci generation and structural parameters for the analyte refractive index from 1.31 to 1.41. We have also shown that the operational sensing wavelengths and sensitivity can be changed significantly by introducing the different Fibonacci sequences in the proposed sensor. The sensing peaks separation, FWHM, and sensitivity can also be tuned by changing the analyte and PC stacked layers' thicknesses. We also introduce the sensing performances for the Blood plasma and Cancer cells detection using the proposed Fibonacci quasiperiodic PC sensor. We observe that the maximum sensitivities and FOM of the proposed sensor are 552.5 nm/RIU and 2986.93 RIU^{-1} for cancer cells and 553.55 nm/RIU and 2214.21 RIU^{-1} for blood plasma, respectively. The proposed structure reveals the tunable sensing performances and stimulates the fabrication interest.

Keywords Fibonacci quasiperiodic sequence · Photonic crystal · Transmittance · Biosensors

✉ Bipin K. Singh
bipinksingh02@gmail.com

[1] Department of Physics, University of Mumbai, Mumbai 400098, India

[2] Department of Science and Humanities, Rajkiya Engineering College, Mainpuri 205001, India

[3] Department of Electronics and Communications, VFSTR, Guntur 522213, India

[4] Department of Physics, Indian Institute of Technology (BHU), Varanasi 221005, India

1 Introduction

Photonic crystals (PCs) with quasiperiodic sequences are very attractive in various theoretical and experimental PC investigations due to their surprising effects, such as more extensive and multiple photonic band gaps (PBGs) with strong self-similarity energy spectrum, and localized states. The exciting properties of the quasiperiodic PCs offer for facilitating to development of various optoelectronic devices, filters, reflectors, switches, and sensors (Steurer and Widmer 2007; Vardeny et al. 2013; Macia 2012). The quasiperiodic structures show the perfect long-range structural ordering between the periodic and disordered media. Compared to the conventional PC structures, more structural configurations are accessible in quasiperiodic PCs to tune their photonic properties (Vyunishev et al. 2017; Singh and Pandey 2018; Padhy et al. 2020). Over the past several years, 1-D PCs with periodic and non-periodic arrangements have been intensively demonstrated with different types of materials for the design of various optical devices and sensors (Temesi et al. 2018; Bonifacio et al. 2009; Wu et al. 2018; Aly et al. 2021; Elsayed et al. 2021; Wu and Gao 2015; Mohebbi 2015). 1-D PC structures are more attractive than 2-D and 3-D PC structures because of their simple fabrication, low cost, and less number of parameters for optimization. One-dimensional quasiperiodic PCs are the most important and convenient design of PC structures because their designs are referred to as stacks of two different layers under the expansion rules of different quasiperiodic sequences. They reveal their optical performance of light and structural modulations in one direction. All the optical properties of electromagnetic waves are often easier to investigate in 1-D PCs. These can be realized in a controlled manner and fabricated more easily for an extensive range of wavelengths and accurate theoretical descriptions. The Fibonacci quasiperiodic PCs are one of the most significant and eminent quasiperiodic PC structures. These quasiperiodic PCs provide efficient and tuneable photonic bandgaps (PBGs), self-similarity energy spectral, and localization phenomena (Poddubny and Lvchenko 2010; Feng et al. 2018; Zhang et al. 2012; Wang et al. 2020; Baghbadorani and Barvestani 2018).

Recently, PCs have been employed as optical sensors for different applications such as temperature, gas, chemical and biological, pressure, and refractive index sensing (Inan et al. 2017; Abohassan et al. 2021; Chaves and Posada 2018; Singh and Pandey 2016). PC structures based sensors are compact, convenient, and highly efficient for real-time monitoring and tunable sensing performances. PC structures with different structural arrangements reveal the privilege to detect various analytes in the temperature, pressure, chemicals, bio-molecular, and cancer cells detections (Abohassan et al. 2021; Chaves and Posada 2018; Singh and Pandey 2016; El-Khozondar et al. 2019; Aly et al. 2020a; Panda and Pukhrambam 2021a). Nowadays, the investigations of the existence of the different kinds of diseases such as cancer, HIV, hepatitis, biochemical and Covid pandemic to the visitation of patients are a challenge in the medical field. The analysis of blood samples performs an important role in the investigation of several diseases. The size and dielectric values for the different diseases affected the blood samples. Blood constituents reveal unique parameters that play an essential role in detecting the different diseases, biochemical and clinical diagnoses (Zhuo et al. 2019; Rohen et al. 2016; Panda and Pukhrambam 2021b; Hu et al. 2020). PC sensors with different structural arrangements, convenient sensing performances, and multi-functionality have been theoretically and experimentally demonstrated using different configurations and techniques (Aly et al. 2020b; Panda et al. 2021; Bayat et al. 2016; Ramanujam et al. 2019; Shen et al. 2016; Dou et al. 2012; Gutierrez et al. 2019). The demonstrations on the influences of different quasiperiodic sequences on

the sensing modes for blood plasma and cancer cells in the quasiperiodic PC sensor have been presented in contracted aspects in the previously reported results (Baghbadorani and Barvestani 2018; Fenzl et al. 2014; Wang et al. 2019). The motive of this work is to demonstrate the sensing response for different structural parameters in one dimensional Fibonacci quasiperiodic PCs for blood plasma and cancer cell detections. Here, the defect mode analysis for various analytes is utilized to invigilate different blood plasmas and cancer cells in terms of refractive indices. The sample layer of different blood plasma concentrations and cancer cells comprises two identical Fibonacci quasiperiodic PCs. The sample layer operates as a defect and exhibits the sensing peaks in the transmission spectra of the proposed structures. The variations in the refractive indices for the blood plasma and the cancer cells reveal a substantial shift in the sensing peaks in the transmission spectra. Thus, it is possible to observe the different blood plasma and cancer cells by inspecting the transmission spectra of the Fibonacci quasiperiodic PCs for different cases.

2 Theoretical description

The schematic diagrams of the proposed sensors based on 1-D Fibonacci quasiperiodic PC structures are shown in Fig. 1 Sensor structures are composed as a multilayers structure of $air/(F_g)^p S(F_g)^p/air$. Here, the subscript g and superscript p represent the generation of Fibonacci quasiperiodic sequence and number of periods, respectively. The considered Fibonacci quasiperiodic generations (F_g) are composed of two variants of layer, A and B. The layered medium A is of the SiO2 with width d_1, and refractive index n_1, and medium B is of the TiO2 with width d_2, and refractive index n_2,. The analyte S is the sample layer

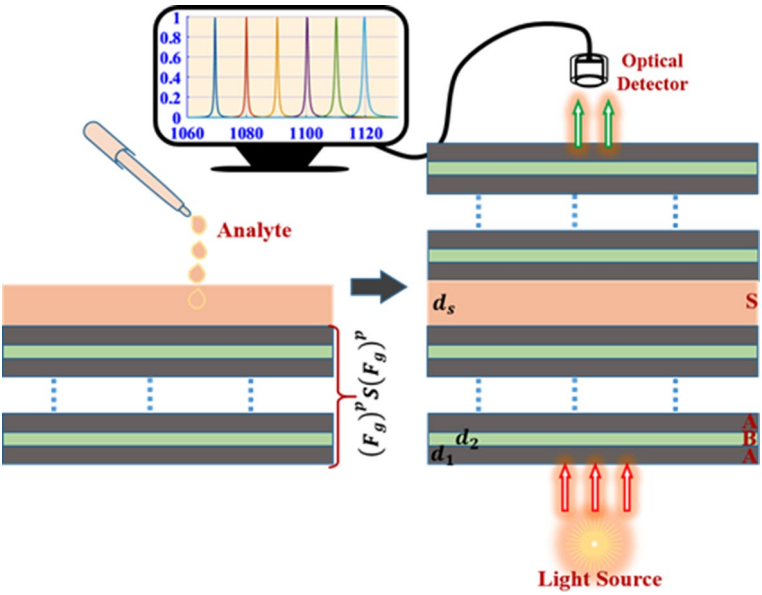

Fig. 1 Schematic diagrams of the proposed 1-D Fibonacci quasiperiodic PC sensor structure of $air/(F_g)^p S(F_g)^p/air$

of width d_s, and refractive index n_s. The Fibonacci quasiperiodic arrangement of layers A and B follow the substitution rule: $A(F_1) \rightarrow AB(F_2) \rightarrow ABA(F_3) \rightarrow ABAAB(F_4) \ldots$ for proceeding generations (g = 1, 2, 3 … so on). The refractive indices of the blood plasma and cancer cell samples are possessed from previously reported results (Abohassan et al. 2021; El-Khozondar et al. 2019; Aly et al. 2020a; Ramanujam et al. 2019). Nowadays, the proposed Fibonacci quasiperiodic PC sensors can be easily fabricated in the multilayer PC structures by utilizing the simplest thin film coating techniques such as spin-coating, doctor-blade, and dip coating approaches, and some advanced and precise thin film coating techniques such as magnetron sputtering and e-beam evaporation etc. (Temesi et al. 2018; Bonifacio et al. 2009; Inan et al. 2017; Shen et al. 2016; Dou et al. 2012; Gutierrez et al. 2019; Fenzl et al. 2014; Wang et al. 2019; Biswas et al. 2012; Shaban et al. 2017).

We have employed the transfer matrix approach to observe the transmission and reflection spectra of the proposed Fibonacci quasiperiodic PC sensor. The interaction between satisfied electric and magnetic fields at input and output regions can interact with the matrix expressions in the multi-layered structures. The amplitudes of the fields for input and output media can be described by the sequential multiplications of the characteristic matrices of the stacked layers as (Wu et al. 2018; El-Khozondar et al. 2019; Aly et al. 2020a; Panda and Pukhrambam 2021a; Singh et al. 2020; Yeh 1988):

$$\begin{pmatrix} C_0 \\ D_0 \end{pmatrix} = M_0^{-1}(M_1.M_2 \ldots M_j)M_0 \begin{pmatrix} C_{j+1} \\ D_{j+1} \end{pmatrix} \tag{1}$$

where j represents the number of media, A_0, B_0 and A_{j+1}, B_{j+1} are the field components for the incident (0th) medium and outgoing (j + 1)th medium, respectively. Matrices $M_j (j = 1, 2, 3 \ldots)$ and M_0 are the 2×2 characteristics matrix of jth medium and air medium, respectively. The characteristic matrices M_j and M_0 for normal incident angle are respectively specified by Wu et al. (2018); El-Khozondar et al. 2019; Aly et al. 2020a; Panda and Pukhrambam 2021a; Singh et al. 2020; Yeh 1988);

$$\left.\begin{aligned} M_j = \begin{bmatrix} \cos\left(\left(\frac{2\pi}{\lambda}\right)n_j d_j\right) & -(i/n_j).\sin\left(\left(\frac{2\pi}{\lambda}\right)n_j d_j\right) \\ -in_j.\sin\left(\left(\frac{2\pi}{\lambda}\right)n_j d_j\right) & \cos\left(\left(\frac{2\pi}{\lambda}\right)n_j d_j\right) \end{bmatrix} \\ M_0 = \begin{bmatrix} 1 & 1 \\ n_0 & -n_0 \end{bmatrix} \end{aligned}\right\} \tag{2}$$

where, n_j and d_j are the layer refractive index and the layer thickness of the jth media. The wavelength of the incident light and the refractive index of air are noted by λ andn_0, respectively. Finally, the transmittance (T) and reflectance (R) of the proposed sensor can be demonstrated by the expressions (Wu et al. 2018; El-Khozondar et al. 2019; Aly et al. 2020a; Panda and Pukhrambam 2021a; Singh et al. 2020; Yeh 1988);$T = \left|\frac{C_{j+1}}{C_0}\right|^2 = \left|\frac{1}{M_{11}}\right|^2$ and$R = \left|\frac{D_0}{C_0}\right|^2 = \left|\frac{M_{21}}{M_{11}}\right|^2$ (3).where, the matrix components M_{11} and M_{21} represent the matrix elements of the resultant matrix $M_{ij}(i, j = 1, 2)$ for the proposed sensor structures. The sensitivity and FOMs are the essential parameters to optimize the performance of the sensor. The sensitivity is calculated by the changes in the sensing peak positions with the change in the sample refractive index, and expressed as (Wu et al. 2018; El-Khozondar et al. 2019; Aly et al. 2020a; Panda and Pukhrambam 2021a):

$$S = \frac{\Delta \lambda_d}{\Delta n_s} \tag{4}$$

The figure of merit (FOM) of the sensor is the ratio of the sensitivity and the full width half maximum (FWHM), and represented as (Wu et al. 2018; El-Khozondar et al. 2019; Aly et al. 2020a; Panda and Pukhrambam 2021a):

$$\text{FOM} = \frac{S}{\text{FWHM}} \tag{5}$$

For designing a convenient sensor with high FOM, we expect high sensitivity and smaller FWHM to sense accurately for small changes in the sample.

3 Results and discussion

To investigate the sensing performance of the 1D Fibonacci quasiperiodic PC sensors, we first explore the detection peaks in the transmission spectra of the proposed sensor for different Fibonacci generations and analytes, as shown in Fig. 2. The refractive indices of SiO_2 (n_1) and TiO_2 (n_2) are possessed from the literature (Gao et al. 2012;

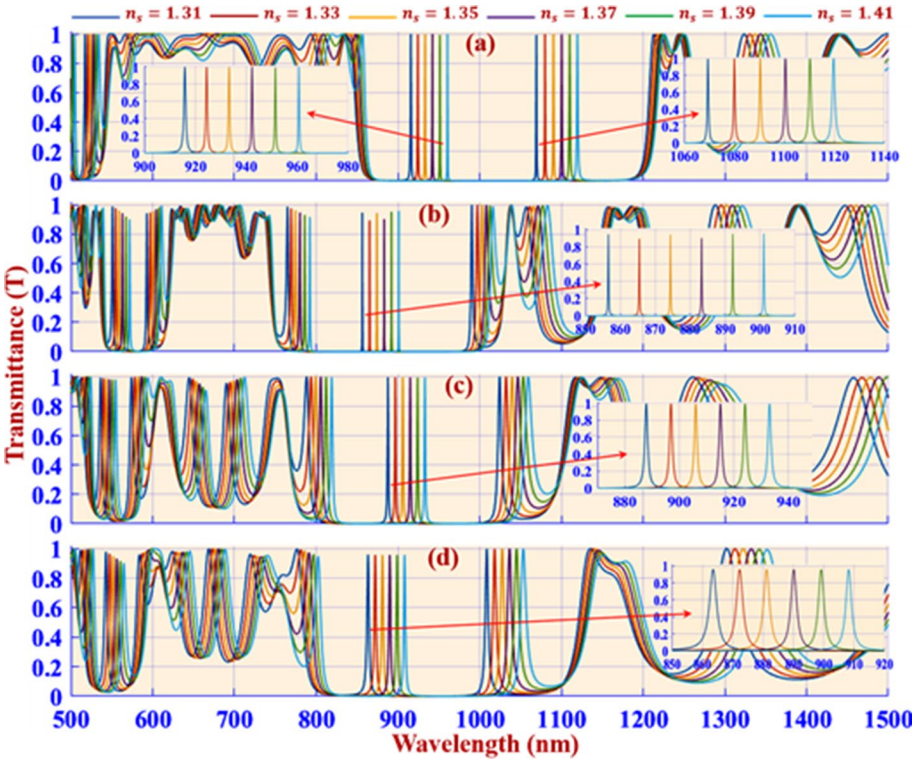

Fig. 2 Transmission spectra of the 1D Fibonacci quasiperiodic PC sensors for the structural arrangements (**a**) $(F_3)^7 S (F_3)^7$, **b** $(F_4)^4 S (F_4)^4$, (c) $(F_5)^2 S (F_5)^2$, and **d** $(F_6)^1 S (F_6)^1$ with different values of analyte refractive index n_S.

Siefke et al. 2016). The thicknesses of layer A (SiO_2) and layer B (TiO_2) are considered $d_1 = 100\,\text{nm}$, $d_2 = 90\,\text{nm}$ respectively. The refractive indices n_1 and n_2 have the values 1.475 and 2.365 for the wavelength 700 nm, respectively. The thickness of the analyte layer is chosen $d_s = 1.5\,\mu\text{m}$. The transmission spectra of the proposed sensors for different Fibonacci generations with the analyte layer refractive index (n_S) variation are shown in Fig. 2. We observe that the transmission band regions and sensing peaks change with different Fibonacci generations in the proposed sensor structures. Different Fibonacci structures conduct to localization of sensing peaks at different positions and in numbers. Here, we obtain the two sensing regions for the sensor structure of $(F_3)^7S(F_3)^7$ and a single sensing region for the other structures of $(F_4)^4S(F_4)^4$, $(F_5)^2S(F_5)^2$, and $(F_6)^1S(F_6)^1$, as can see in Fig. 2(a), (b), (c) and (d), respectively. The sensing peaks positions (λ_p) have variations toward higher wavelength with increasing the values of n_S. The separation insight of the sensing peaks position (λ_p) for different n_S-values and Fibonacci generations are depicted in the insets in the corresponding figures. We observe that the proposed PC sensor structures with different Fibonacci sequences reveal the efficient variations of sensing peak position for different values of composing layers according to the Fibonacci sequences and have the potential to design effective 1D PC sensors. We have also studied the transmission spectra for the structure with periodic arrangements. We have compared the results with different Fibonacci quasiperiodic sequences based structures with the same layer thickness and the total number of layers. In some cases, structures have the same number of layers and thicknesses. However, structures have slightly changed these values in others because of the odd number of layers for different Fibonacci sequences. We observed that the Fibonacci sequence-based PC structures reveal efficient sensing performance compared to the structures with periodic arrangements for the same lattice parameters. So, we have not incorporated the results for the structures with periodic arrangements for the same lattice parameters. We have incorporated the best-optimized results in the sensing performances for the Fibonacci sequence-based PC sensor structures.

For the different Fibonacci structures and analyte refractive indices, the sensing peak positions(λ_p), sensitivity, and FOMs have variations. To look closely at such variations, we plot the graph for λ_p withn_S, sensitivity, and FOMs with Δn_S in Fig. 3 for the sensor structures with different Fibonacci generations. From the Fig. 3(a)–(d), we observe that the sensing peak positions λ_p shift toward higher wavelength with n_S-values for all the cases. The variations of λ_p with n_s are linear, but they reveal dissimilar slope transformations for different Fibonacci generations. For the sensor structure of $(F_3)^7S(F_3)^7$, the sensitivity and FOM for the first order and second order sensing peaks, respectively, increases and decreases with Δn_S, as shown in Fig. 3(e). Here, Δn_S represents the difference of two respective refractive indices as the value of $n_{21}(= 1.33 - 1.31)$, $n_{32}(= 1.35 - 1.33)$, $n_{43}(= 1.37 - 1.35)$, $n_{54}(= 1.39 - 1.37)$, $n_{54}(= 1.39 - 1.37)$, $n_{54}(= 1.39 - 1.37)$, and $n_{65}(= 1.41 - 1.39)$. Layer thicknesses are $d_1 = 100\,\text{nm}$, $d_2 = 90\,\text{nm}$, and $d_s = 1.5\,\mu\text{m}$. Maximum sensitivity and FOMs of the sensor with $\left(F_3\right)^7S\left(F_3\right)^7$ are, respectively, 465 nm/RIU and 1033.33 RIU^{-1} for the first order peaks and 530 nm/RIU and 963.64 RIU^{-1} for the second order peaks. For the other sensor structures of $\left(F_4\right)^4S\left(F_4\right)^4$, $\left(F_5\right)^2S\left(F_5\right)^2$, and $\left(F_6\right)^1S\left(F_6\right)^1$, the sensitivity and FOM are randomly change with Δn_S as shown in Fig. 3(f), (g) and (h), respectively. The changes in the sensing peaks and sensitivity are the results of the changes in the structural arrangements for the different Fibonacci generations. The FOMs vary due to changes in the full-width half maxima (FWHM) of sensing peaks under the influence of the different Fibonacci sequences. For all cases, as shown in Fig. 3, we

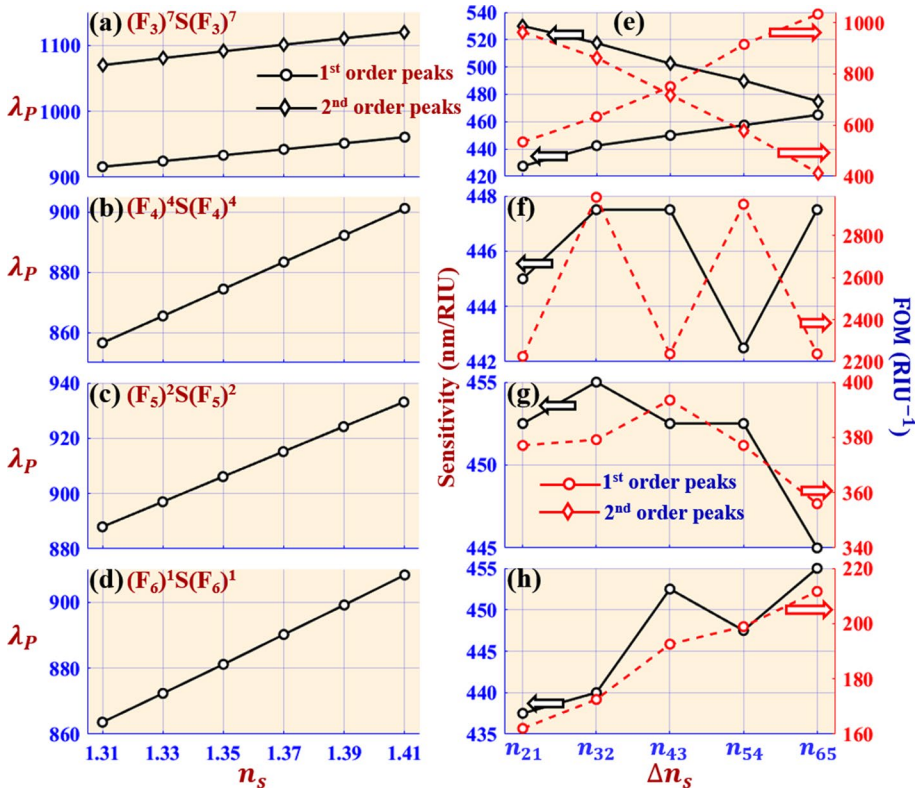

Fig. 3 **a**–**d** the variation of sensing peak positions λ_p with analyte refractive index n_s, and **e**–**h** the variations of sensitivity and figure of merit (FOM) with the difference of two corresponding refractive indices parameter Δn_S

obtain the maximum sensitivity of 530 nm/RIU and the maximum FOM of 2983.33 RIU-1. The remarkable modification and high sensitivity and FOM values offer an approach to realize the potential refractive index sensors.

To examine the effect arising on the variations of sensing peaks due to the different Fibonacci generations periodicity (p), we have depicted the transmission spectra for the sensor structures of $(F_3)^p S(F_3)^p$, $(F_4)^p S(F_4)^p$, $(F_5)^p S(F_5)^p$, and $(F_6)^p S(F_6)^p$ with different values of the periodicity (p) in Fig. 4. We observe that the sensing peak positions are the same for all the cases with different periodicities, but their FWHM and intensity change with periodicity. The changes in the FWHM and intensity show the diverse behavior for the different Fibonacci generations. It is the result of the different layer numbers and their staking under different Fibonacci generations. The intensity of the sensing peaks decreases to a minimum with the periodicity as proceed to the higher-order Fibonacci generations. The FWHMs are also become narrower with increasing the periodicity. The remarkable variations in the intensity and FWHM of the sensing peaks induce the optimized periodicity for different generations.

To optimize the thicknesses constituted layers in the sensor structures, we have demonstrated the transmission spectra for the layers thickness d_s, d_1, and d_2 in Figs. (5) – (7), respectively, with sensor structures of the 3rd, 4th and 5th Fibonacci generations. As per

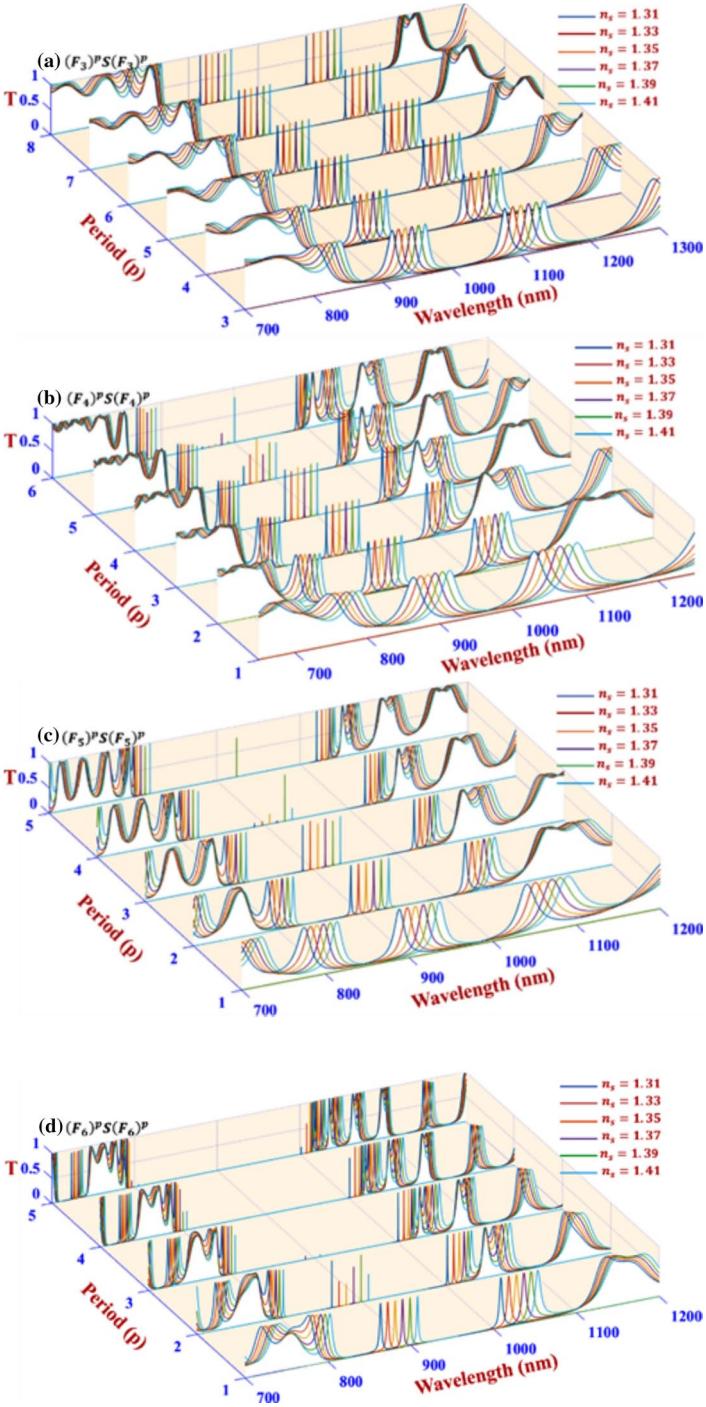

Fig. 4 Transmission spectra of the sensors for structural arrangements (**a**) $(F_3)^P S(F_3)^P$, **b** $(F_4)^P S(F_4)^P$, **c** $(F_5)^P S(F_5)^P$, and **d** $(F_6)^P S(F_6)^P$ with different periodicities (p) and analyte refractive index n_S.

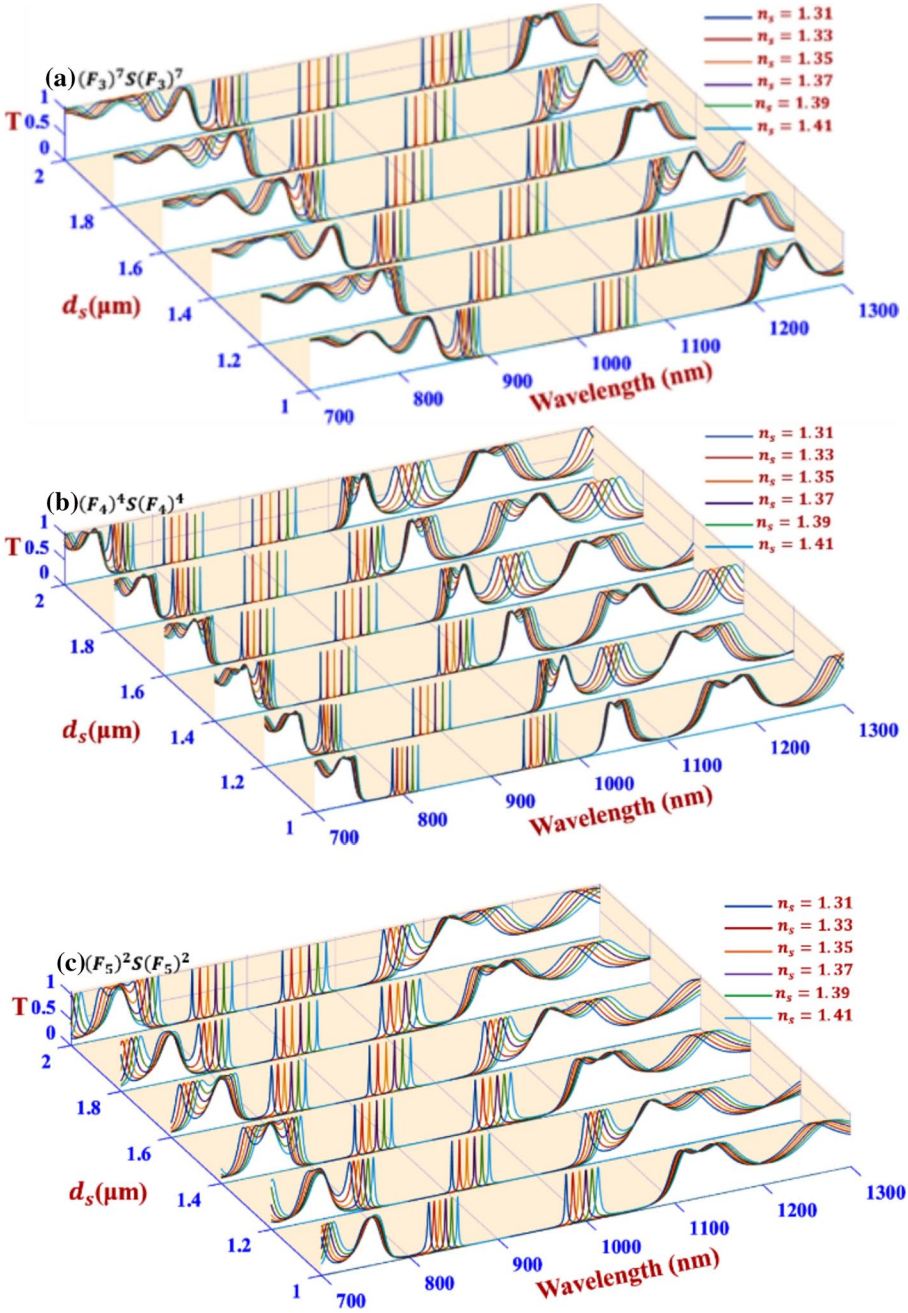

Fig. 5 Transmission spectra of the sensors for the structure of (**a**) $(F_3)^7S(F_3)^7$, **b** $(F_4)^4S(F_4)^4$, **c** $(F_5)^2S(F_5)^2$ for the variations of layer thickness d_s with different values of n_S.

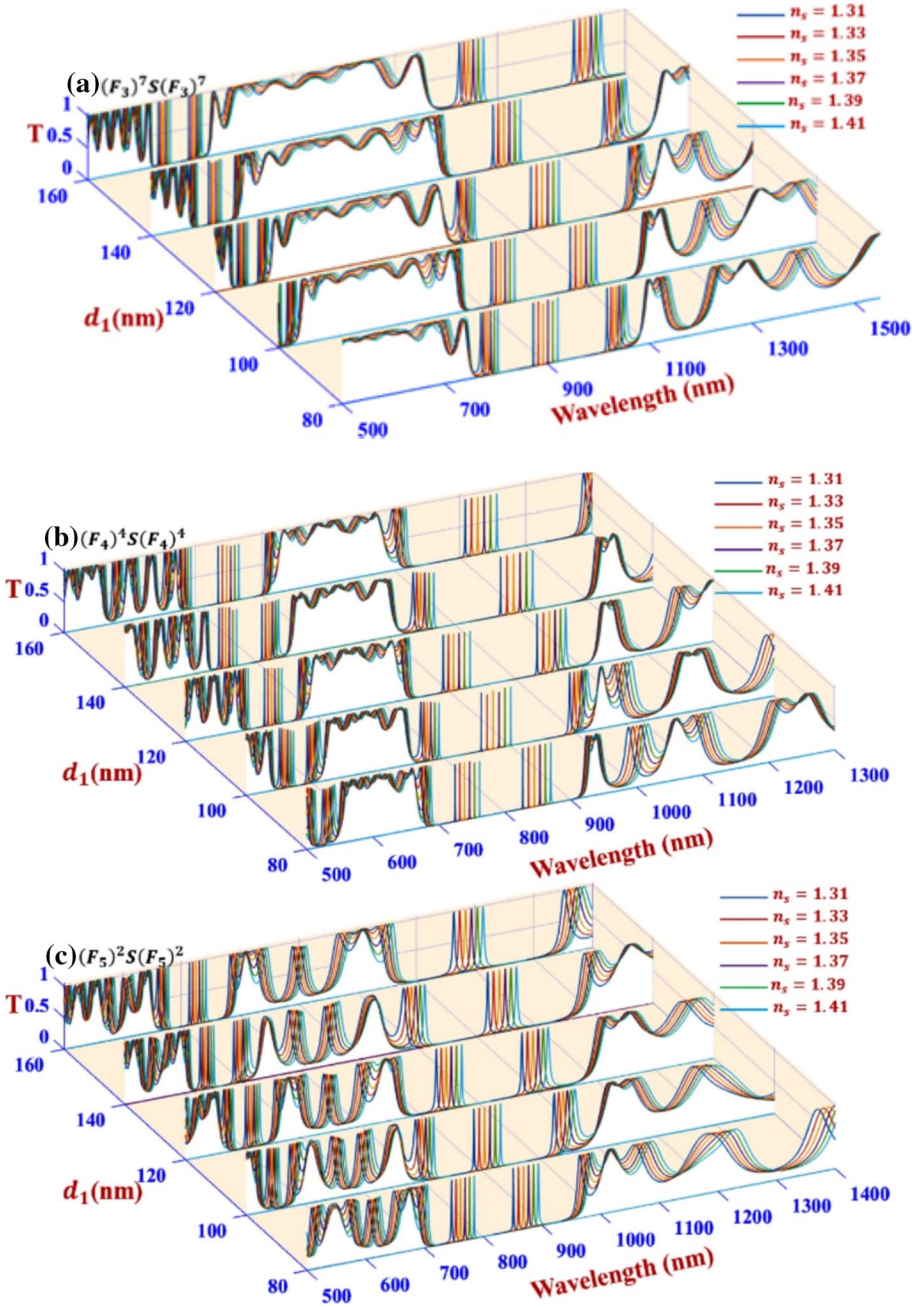

Fig. 6 Transmission spectra of the sensors for the structure of (**a**) $(F_3)^7S(F_3)^7$, **b** $(F_4)^4S(F_4)^4$, **c** $(F_5)^2S(F_5)^2$ for the variations of layer thickness d_1 with different values of n_S.

the above results, we have preferred the periodicity (p) 7, 4, and 2 for the 3rd, 4th, and 5th Fibonacci generations, respectively. In Fig. 5, we have shown the transmission spectra and the transformation of sensing peaks for the variation of sample layer thicknesses d_s from 1 μm to 2 μm with different values of n_S, and $d_1 = 100nm$ $\mathrm{d}_1 = 100$ nm $\mathrm{d}_1 = 100$nm and $d_2 = 90\ nm$ $d_2 = 90\ nm$ $d_2 = 90\ nm$. The separations and position of the sensing peaks show the noticeable changes with increasing the value of d_s for all cases. We observe that the FWHMs of the sensing peaks also change with d_s. The Fibonacci sequence generations also show the considerable effect on the separations, positions, and FWHMs of the sensing peaks, as depicted in Figs. 5(a), (b), and (c) for the sensor structures of $(F_3)^7S(F_3)^7$ $(\mathrm{F}_3)^7\mathrm{S}(\mathrm{F}_3)^7$ $(\mathrm{F}_3)^7\mathrm{S}(\mathrm{F}_3)^7$, $(F_4)^4S(F_4)^4$ $(\mathrm{F}_4)^4\mathrm{S}(\mathrm{F}_4)^4$ $(\mathrm{F}_4)^4\mathrm{S}(\mathrm{F}_4)^4$, and $(F_5)^2S(F_5)^2$ $(\mathrm{F}_5)^2\mathrm{S}(\mathrm{F}_5)^2$ $(\mathrm{F}_5)^2\mathrm{S}(\mathrm{F}_5)^2$, respectively. With the variation in the values of d_s, the sensitivity and FOMs change due to the transformation in the separation and FWHM of the sensing peaks for different Fibonacci generations.

A similar investigation has also been carried out to reveal the impact of layer thicknesses d_1 and d_2 on the sensing performance, and demonstrated in Figs. (6) and (7), respectively. We have considered the layer thickness d_1 varies from 80 to 160 nm, and other layer thickness fixed as $d_2 = 90nm$ and $d_s = 1.5\mu m$ for Fig. (6) and chosen the layer thickness d_2 from 60 to 140 nm with the fixed values of $d_1 = 100nm$ and $d_s = 1.5\mu m$ for Fig. 7. It can be seen that the transmittance band and sensing peaks shift toward higher wavelength with increasing the values of d_1 and d_2 for all cases of n_S. The changes in the transmission spectra and sensing peak performances under the influence of the Fibonacci generation can be viewed in sections (a), (b), and (c) of Figs. (6) and (7), respectively. One can see that the separation, position, and FWHM of the sensing peaks depend on the sample layer thickness, constituted PC layer thickness with different Fibonacci generation. Thus, a substantial quantity of the sample is required for getting considerable sensitivity. These results induce consideration of the appropriate structural parameters with the different Fibonacci sequences for efficient sensing performance.

We have demonstrated all the above results for the analyte refractive index range from 1.31 to 1.41 because the refractive indices for most bio-fluids such as hemoglobin, glucose in the blood, blood plasma, cancer cells, etc., possess in this range (El-Khozondar et al. 2019; Zhuo et al. 2019; Rohen et al. 2016; Aly et al. 2020b; Panda et al. 2021; Bayat et al. 2016; Ramanujam et al. 2019). Therefore, the introduced Fibonacci quasiperiodic PC sensor can be employed for bio-sensing. To explore the utility of the proposed sensor as a bio-sensor, we reveal here the characteristics of the sensor for blood plasma and cancers cell sensing applications. We have picked the refractive indices for the different concentrated blood plasma from Ref. (El-Khozondar et al. 2019; Rohen et al. 2016; Bijalwan et al. 2021). Figure 8 shows the transmission spectra with the variations of sample layer for different concentrations of blood plasma in the sensor with different Fibonacci generations. The sensing peaks shift toward the higher wavelength with increasing the blood plasma concentrations for all cases. It is the result of the change in the blood sample refractive index with different plasma concentrations. It can also be seen that the separation, position, and FWHM of the sensing peaks for different concentrations change with tuning the sample layer thickness and Fibonacci generations in the sensor structures.

To look closely at the variations of sensing peaks for different plasma concentrations, sample thickness, and Fibonacci generations, we have revealed the sensing peak λ_p shifting with the blood plasma concentrations in panel (i) of Fig. 9. The changes in the position of λ_p with the concentrations C_{BP} are linear for all the cases, but they illustrate slightly dissimilar slope transformations for different layer thicknesses and Fibonacci

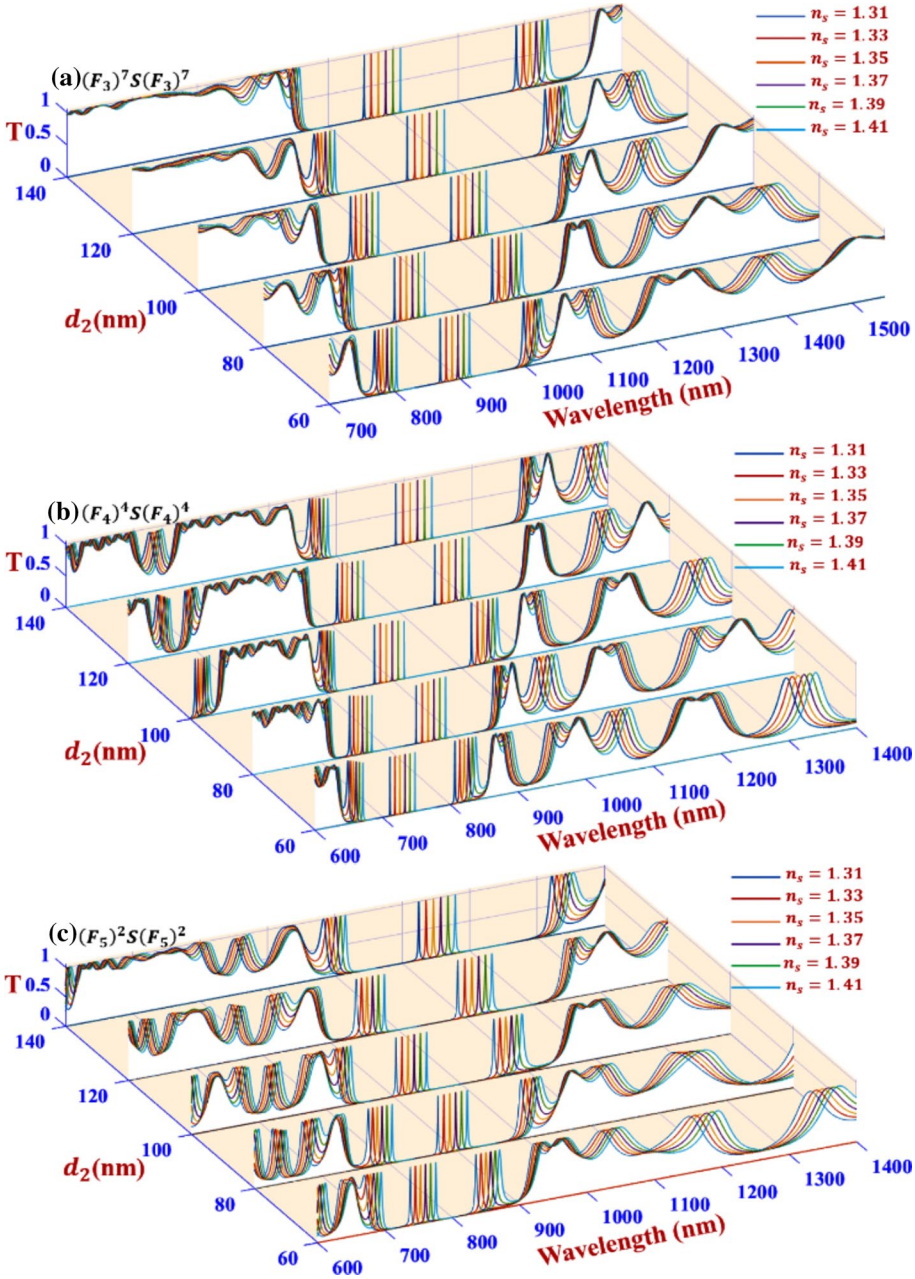

Fig. 7 Transmission spectra of the sensors for the structure of (**a**) $(F_3)^7S(F_3)^7$, **b** $(F_4)^4S(F_4)^4$, **c** $(F_5)^2S(F_5)^2$ for the changes in layer thickness d_2 with different values of n_S.

generations. To examine the sensing performance of the senor for blood plasma, we have calculated the sensitivity and FOM for different concentrations contrast ΔC_{BP} by taking the blood plasma concentration of 10 g/L as a reference and shown in the panels (ii) and

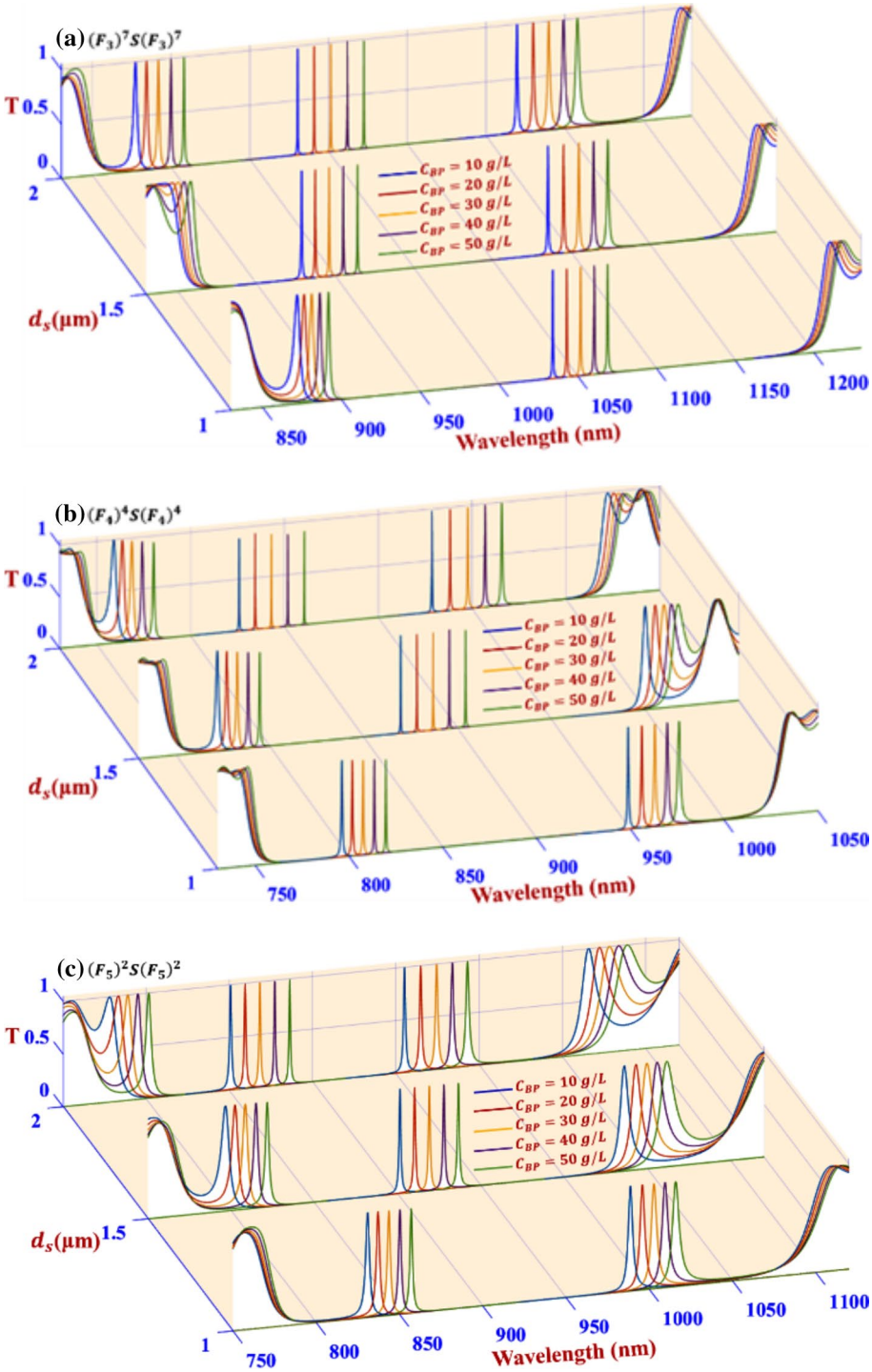

Fig. 8 Transmission spectra of the sensors for the structure of (**a**) $(F_3)^7S(F_3)^7$, **b** $(F_4)^4S(F_4)^4$, **c** $(F_5)^2S(F_5)^2$ for the changes in layer thickness d_s with different blood plasma concentrations C_{BP}

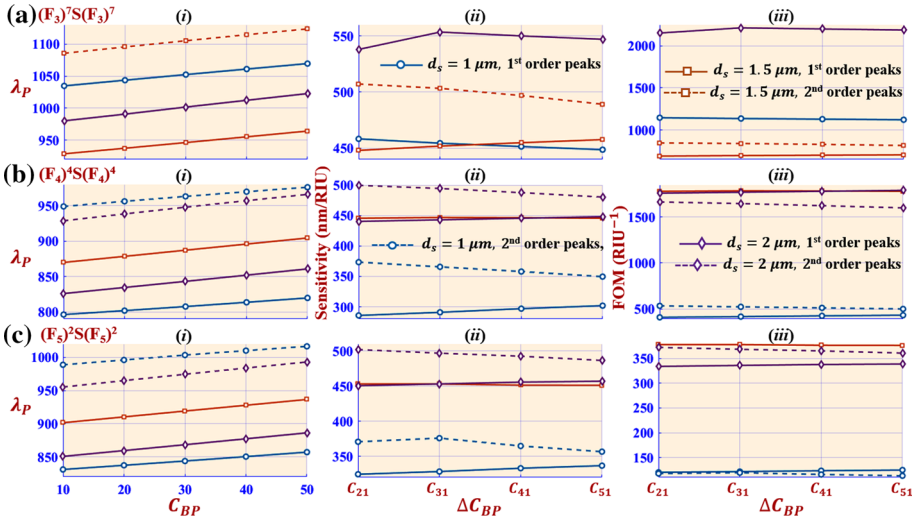

Fig. 9 The variations of (panel-i) the sensing peak λ_p positions with blood plasma concentrations C_{BP}, (panel-ii) the sensitivity, and (panel-iii) the FOM with the concentrations contrast ΔC_{BP} by taking the blood plasma concentration of 10 g/L as a reference for the sensor structures of (**a**) $(F_3)^7 S(F_3)^7$, **b** $(F_4)^4 S(F_4)^4$, **c** $(F_5)^2 S(F_5)^2$, respectively

(iii) of Fig. 9, respectively. Here, ΔC_{BP} represents the concentrations contrast for the blood plasma concentration of 10 g/L as a reference, and the values of different concentrations contrast are $C_{21}(= C_{20g/L} - C_{10g/L})$, $C_{31}(= C_{30g/L} - C_{10g/L})$, $C_{41}(= C_{40g/L} - C_{10g/L})$, and $C_{51}(= C_{50g/L} - C_{10g/L})$. Layer thicknesses are $d_1 = 100\ nm, d_2 = 90\ nm$, and $d_s = 1\ mum, 1.5\ mum, 2.0\ mum$. The maximum sensitivity and FOM are 553.55 nm/RIU and 2214.21 RIU^{-1} for the sensor structures $(F_3)^7 S(F_3)^7$, 499.5 nm/RIU and 1791.97 RIU^{-1} for the sensor $(F_4)^4 S(F_4)^4$, 502.05 nm/RIU and 377.62 RIU^{-1} for the structure $(F_5)^2 S(F_5)^2$, respectively. It can be seen in the figure that the sensitivity and FOM have remarkable variations with the concentrations contrast, sample layer thickness, and Fibonacci generation, but the FOM reveals a drastic variation concerning the change in the Fibonacci generations for the sensor structures. As per the results, we observe the efficient higher sensitivity with maximum value 553.55 nm/RIU and FOMs with maximum value 2214.21 RIU^{-1} for the blood plasma compared to the previously reported results in Refs. (El-Khozondar et al. 2019; Aly et al. 2020b; Bijalwan et al. 2021). The diversity in the sensing performance of the proposed sensors in terms of sensing peak separations, high sensitivity, and FOM induce to utilize as a highly efficient and tunable sensor for the blood plasma detections.

Now, we have carried out our analysis on the detection of cancer cells. We have considered the sample size and refractive index of the cancer cells according to the previously reported results (Abohassan et al. 2021; El-Khozondar et al. 2019; Zhuo et al. 2019; Panda et al. 2021; Ramanujam et al. 2019; Bijalwan et al. 2021). Figure 10 shows the transmission spectra of the sensor structures of (a) $(F_3)^7 S(F_3)^7$, (b) $(F_4)^4 S(F_4)^4$, (c) $(F_5)^2 S(F_5)^2$ for the different cancer cells with the sample layer thicknesses. Here, layer thicknesses are also considered as $d_1 = 100\ nm, d_2 = 90\ nm$, and $d_s = 1\ mum$, $1.5\mu\ m$, $2.0\mu\ m$. The sensing peaks shift toward the higher wavelength for all cases with the incorporation of the cancer cell. The changes in the peak position are the result of the change in the refractive index for

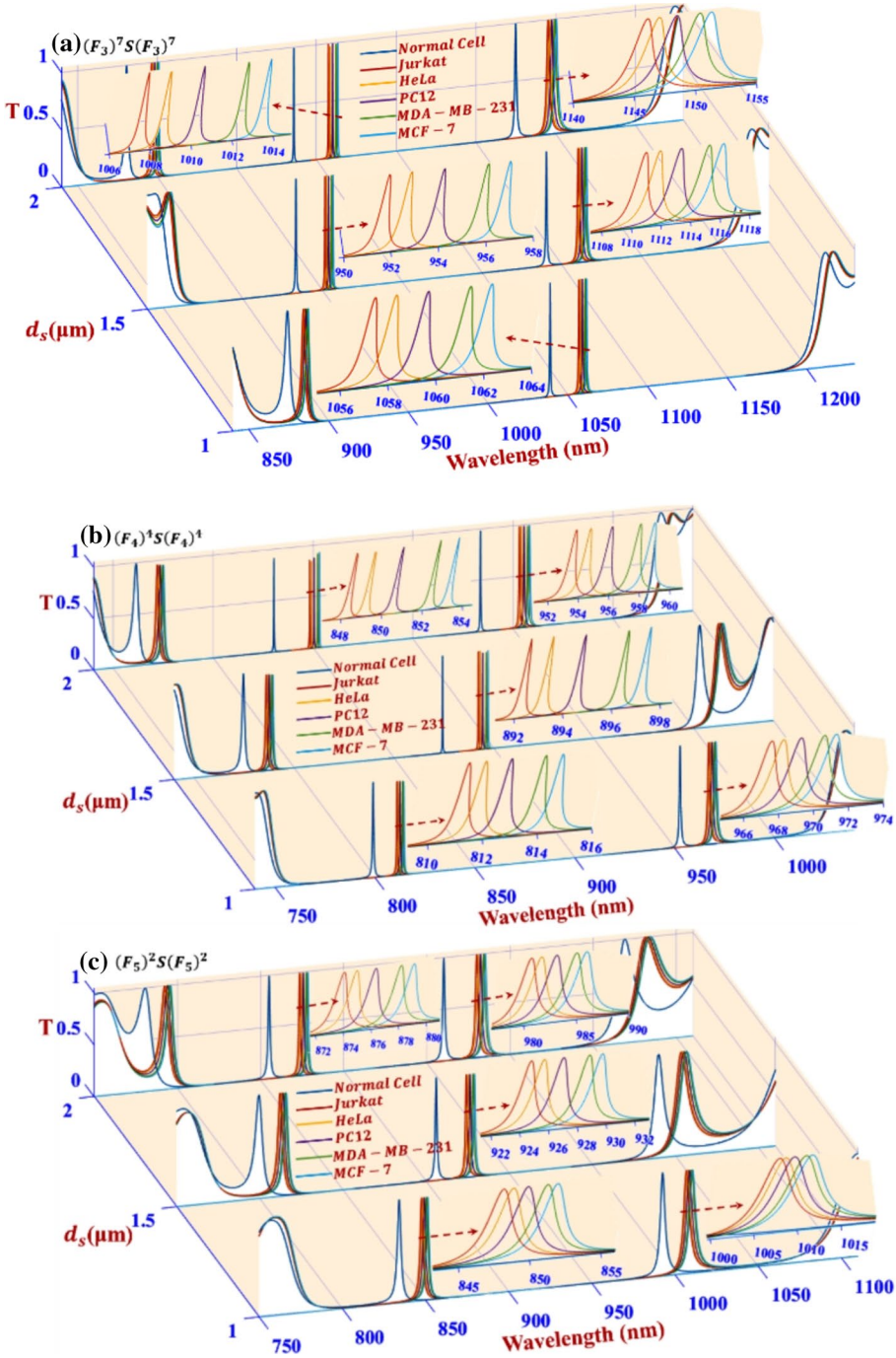

Fig. 10 Transmission spectra of the sensors structure of (**a**) $(F_3)^7S(F_3)^7$, b $(F_4)^4S(F_4)^4$, **c** $(F_5)^2S(F_5)^2$ with the changes in sample layer thickness d_s for different cancer cells sample

different cancer cells. We can see that the separation, position, and FWHM of the sensing peaks for different cancer cells change with tuning the sample layer thickness and Fibonacci generations in the sensor structures. Here, we have considered the normal cell with refractive index 1.35 and different cancer cells of Jurkat, Hela, PC12, MDA-MB-231, and MCF-7 with refractive indices 1.39, 1.392, 1.395, 1.399, and 1.401, respectively. To take a close look at the variations of the sensing peaks for different cancer cells with respect to the normal cell, we have zoom out the sensing peaks and depicted them in the insets of the respective figures.

The variations in the sensing peaks λ_p correspond to the various cancer cells, and sensitivity and FOM for the different cancer cells with the normal cell as a reference are shown in Fig. 11. We also reveal here that the position of sensing peaks shifts toward the higher wavelength with tuning the refractive index n_C from the normal cell to cancel cells for all the cases. The slops of the λ_p vs. n_C are almost linear for all the cases, but the separations in the sensing peaks for different cancer cells have different values for the sample layer thickness and Fibonacci generations. To look into the sensing performance, we have calculated the sensitivity and FOMs for different cancer cells with the normal cell as a reference, and this transformation is represented as Δn_{CN} $(= n_{\text{cancercell}} - n_{\text{normalcell}})$. The changes in Δn_{CN} for the cancer cell of Jurkat, Hela, PC12, MDA-MB-231, and MCF-7 are 0.04, 0.042, 0.045, 0.049, and 0.0501, respectively. The variations in the sensitivity and FOMs with Δn_{CN} are shown in panels (ii) and (iii) of Fig. 11 for the sensor structures of (a) $(F_3)^7S(F_3)^7$, (b) $(F_4)^4S(F_4)^4$, (c) $(F_5)^2S(F_5)^2$, respectively. The maximum sensitivity and FOMs are 552.5 nm/RIU and 2210 RIU^{-1} for the sensor structures of $(F_3)^7S(F_3)^7$, 486.25 nm/RIU and 2986.93 RIU^{-1} for the sensor of $(F_4)^4S(F_4)^4$, and 491.25 nm/RIU and 393.48 RIU^{-1} for the structure $(F_5)^2S(F_5)^2$, respectively. We can see in the figures that the sensitivity and FOMs have considerable changes with the cancer cells verity, sample

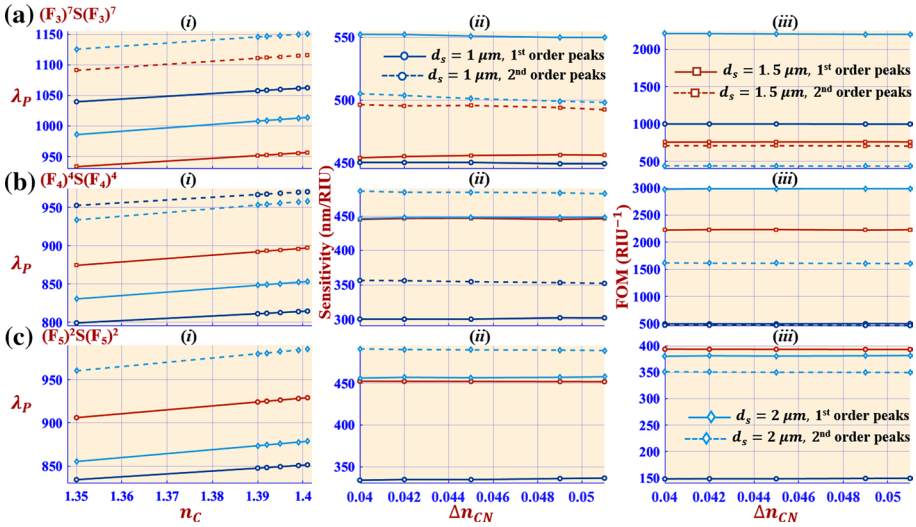

Fig. 11 The variations of (panel-i) the sensing peak λ_p positions with the cancer cell refractive index n_C, (panel-ii) the sensitivity, and (panel-iii) the FOMs with Δn_{CN} by taking the normal cell as a reference for the sensor structures of (**a**) $(F_3)^7S(F_3)^7$, **b** $(F_4)^4S(F_4)^4$, **c** $(F_5)^2S(F_5)^2$, respectively

layer thickness, and Fibonacci generation. However, the FOM has a drastic variation for the change in the Fibonacci generations for the sensor structures. We obtain the sufficient higher sensitivity with maximum value 552.5 nm/RIU and FOMs with maximum value 2986.93 RIU^{-1} for the corresponding cancer cells compared to the previously reported results in Refs. (Abohassan et al. 2021; Zhuo et al. 2019; Panda et al. 2021; Ramanujam et al. 2019; Bijalwan et al. 2021). The calculated sensitivity and FOMs describe the potential of the Fibonacci quasiperiodic PC sensor as a highly efficient and tunable sensor for cancer cells detectio.

4 Conclusion

We have presented the Fibonacci quasiperiodic PC-based sensor and demonstrated the effect of the layer thickness and Fibonacci generation on the sensing performance of the senor. It is observed that the sensing peak positions and active sensing wavelength regions can be tuned by selecting the applicable constituted layer thickness and Fibonacci generation. The sensitivity and FOMs can also modulate by adjusting the layer thickness and Fibonacci generation of the sensor structures. We have observed that the sensitivity and FOMs of the proposed sensor can be modulated from 427.5 nm/RIU to 530 nm/RIU and 162.5 RIU^{-1} to 2983.33 RIU^{-1} by adopted the pertinent sensor structures with Fibonacci generation and structural parameters. Further, we have demonstrated the application of such PC sensors as the blood plasma and cancer cells detections. Sensitivity and FOMs have been obtained to be modulated from 285.79 nm/RIU to 553.55 nm/RIU and from 113.2 RIU^{-1} to 2214.21 RIU^{-1} for blood plasma, and from 300 nm/RIU to 552.5 nm/RIU and from 148.33 RIU^{-1} to 2986.93 RIU^{-1} for cancer cells detections, respectively. This modulation can be regulated by employed the appropriate sensor structures with Fibonacci generation and structural parameters. The demonstrated sensing performances of the considered PC sensors describe their potential for effectively detecting the blood plasma, cancer cells, and other such type bio-analyses.

Acknowledgements Bipin K. Singh is thankful to the University Grants Commission (UGC), India, for providing financial support in the form of Dr. D S K Postdoctoral Fellowship.

Authors contributions All the authors have significant contribution in this paper.

Funding The authors received no specific funding for this work.

Data availability Data and code of this work will available from the corresponding author upon reasonable request.

Declarations

Conflict of interests The authors declare no competing interests.

Ethics approval Not Applicable.

Consent to participate Not Applicable.

Consent to publish Not Applicable.

References

Abohassan, K.M., Ashour, H.S., Abadla, M.M.: A 1D photonic crystal-based sensor for detection of cancerous blood cells. Opt Quant Electron **53**, 356–369 (2021)

Aly, A.H., Mohamed, D., Mohaseb, M.A., ElGawaad, N.S.A., Trabelsi, Y.: Biophotonic sensor for the detection of creatinine concentration in blood serum based on 1D photonic crystal. RSC. Adv. **10**, 31765–31772 (2020)

Aly, A.H., Zaky, Z.A., Shalaby, A.S., Ahmed, A.M., Vigneswaran, D.: Theoretical study of hybrid multifunctional one-dimensional photonic crystal as a flexible blood sugar sensor. Phys. Scr. **95**, 035510 (2020)

Aly, A.H., Awasthi, S.K., Mohamed, D., Matar, Z.S., Al-Dossarid, M., Amin, A.F.: Study on a one-dimensional defective photonic crystal suitable for organic compound sensing applications. RSC Adv. **11**, 32973–32980 (2021)

Baghbadorani, H.K., Barvestani, J.: Effect of uniaxial strain on the performance of one-dimensional graphene Fibonacci photonic crystal biosensors. J. Lightwave. Technol. **36**, 5406–5412 (2018)

Bayat, F., Kandjani, S.A., Tajalli, H.: Designing real-time biosensors and chemical sensors based on defective 1-D photonic crystals. IEEE. Photonic. Technol. Lett. **28**, 1843–1846 (2016)

Bijalwan, A., Singh, B.K., Rastogi, V.: Analysis of one-dimensional photonic crystal based sensor for detection of blood plasma and cancer cells. Optik. **226**, 165994 (2021)

Biswas, A., Bayer, I.S., Biris, A.S., Wang, T., Dervishi, E., Faupel, F.: Advances in top–down and bottom–up surface nanofabrication: techniques, applications & future prospects. Adv. Coll. Int. Sci. **170**, 2–27 (2012)

Bonifacio, L.D., Lotsch, B.V., Puzzo, D.P., Scotognella, F., Ozin, G.A.: Stacking the nanochemistry deck: structural and compositional diversity in one-dimensional photonic crystals. Adv. Mater. **21**, 1641–1646 (2009)

Chaves, F.S., Posada, H.V.: Dependence of the defect mode with temperature, pressure and angle of incidence in a 1D semiconductor-superconductor photonic crystal. Phys. c: Supercond. Appl. **553**, 1–7 (2018)

Dou, Y., Han, J., Wang, T., Wei, M., Evans, D.G., Duan, X.: Fabrication of MMO–TiO_2 one dimensional photonic crystal and its application as a colorimetric sensor. J. Mater. Chem. **22**, 14001–14007 (2012)

El-Khozondar, H.J., Mahalakshmi, P., El-Khozondar, R.J., Ramanujam, N.R., Amiri, I.S., Yupapin, P.: Design of one dimensional refractive index sensor using ternary photonic crystal waveguide for plasma blood samples applications. Phys. e: Low-Dim. Syst. Nanostr. **111**, 29–36 (2019)

Elsayed, H.A., Sharma, A., Alrowaili, Z.A., Taha, T.A.: Theoretical investigation of pressure sensing using a defect of polystyrene inside photonic crystals. Mater. Chem. Phys. **270**, 124853 (2021)

Feng, Y., Liu, Y., Wang, X., et al.: Tunable multichannel plasmonic filter based on a single graphene sheet on a fibonacci quasiperiodic structure. Plasmonics **13**, 653–659 (2018)

Fenzl, C., Hirsch, T., Wolfbeis, O.S.: Photonic crystals for chemical sensing and biosensing. Angew. Chem. Int. Ed. **53**, 3318–3335 (2014)

Gao, L., Lemarchand, F., Lequime, M.: Exploitation of multiple incidences spectrometric measurements for thin film reverse engineering. Opt. Express **20**, 15734–15751 (2012)

Gutierrez, C.F.R., Hernandez, H.D.M., Cabrera, I.A.L., García, M.E.R.: Design, fabrication, and optical characterization of one-dimensional photonic crystals based on porous silicon assisted by in-situ photoacoustics. Sci. Rep **9**, 14732 (2019)

Hu, C., Zhang, H., Ma, Y.: Temperature-switchable mode selector in superconducting photonic crystals based on the Thue-Morse sequence". J. Opt. Soc. Am. B **37**, 287–294 (2020)

Inan, H., Poyraz, M., Inci, F., Lifson, M.A., Baday, M., Cunningham, B.T., Demirci, U.: Photonic crystals: emerging biosensors and their promise for point-of-care applications. Chem. Soc. Rev. **46**, 366–388 (2017)

Macia, E.: Exploiting aperiodic designs in nanophotonic devices. Rep. Prog. Phys. **75**, 036502 (2012)

Mohebbi, M.: Refractive index sensing of gases based on a one-dimensional photonic crystal nanocavity. J. Sens. Sens. Syst. **4**, 209–215 (2015)

Padhy, A., Bandyopadhyay, R., Costa, C.H., Bezerra, C.G., Nayak, C.: Enhanced transmission induced by embedded graphene in periodic, quasiperiodic, and random photonic crystals. J. Optic. Soc. Am. B **37**, 3801–3808 (2020)

Panda, A., Pukhrambam, P.D.: Investigation of defect based 1D photonic crystal structure for real-time detection of waterborne bacteria. Physica B **607**, 412854 (2021)

Panda, A., Pukhrambam, P.D.: A theoretical proposal of high performance blood components biosensor based on defective 1D photonic crystal employing WS_2, MoS_2 and graphene. Opt. Quant. Electron. **53**, 357 (2021b)

Panda, A., Pukhrambam, P.D., Wu, F., Belhadj, W.: Graphene-based 1D defective photonic crystal biosensor for real-time detection of cancer cells. Eur. Phys. J. plus **136**, 809–828 (2021)
Poddubny, A.N., Lvchenko, E.L.: Photonic quasicrystalline and aperiodic structures. Physica. E. **42**, 1871–1895 (2010)
Ramanujam, N.R., Amiri, I.S., Taya, S.A., Olyaee, S., Udaiyakumar, R., Pandian, A.P., Wilson, K.S.J., Mahalakshmi, P., Yupapin, P.P.: Enhanced sensitivity of cancer cell using one dimensional nano composite material coated photonic crystal. Microsyst. Technol. **25**, 189–196 (2019)
Rohen, A.N., Tello, H.C., Luna, G.M., Valenzuela, A.G.: On the effective refractive index of blood. Phys. Script. **91**, 015503 (2016)
Shaban, M., Ahmed, A.M., Rahman, E.A., Hamdy, H.: Tunability and sensing properties of plasmonic/1D photonic crystal. Sci. Rep. **7**, 41983 (2017)
Shen, H., Wang, Z., Wu, Y., Yang, B.: One-dimensional photonic crystals: fabrication, responsiveness and emerging applications in 3D construction. RSC. Adv. **6**, 4505–4520 (2016)
Siefke, T., Kroker, S., Pfeiffer, K., Puffky, O., Dietrich, K., Franta, D., Ohlídal, I., Szeghalmi, A., Kley, E.B., Tünnermann, A.: Materials pushing the application limits of wire grid polarizers further into the deep ultraviolet spectral range. Adv. Opt. Mater. **4**, 1780–1786 (2016)
Singh, B.K., Pandey, P.C.: Effect of temperature on terahertz photonic and omnidirectional band gaps in one-dimensional quasi-periodic photonic crystals composed of semiconductor InSb. Appl. Opt. **55**, 5684–5692 (2016)
Singh, B.K., Pandey, P.C.: Tunable temperature-dependent THz photonic bandgaps and localization mode engineering in 1D periodic and quasi-periodic structures with graded-index materials and InSb. Appl. Opt. **57**, 8171–8181 (2018)
Singh, B.K., Bambole, V., Rastogi, V., Pandey, P.C.: Multi-channel photonic bandgap engineering in hyperbolic graded index materials embedded one-dimensional photonic crystals. Opt. Laser. Technol. **129**, 106293 (2020)
Steurer, W., Widmer, S.: Photonic and phononic quasicrystals. J. Phys. D **40**, R229–R247 (2007)
Temesi, K.S., Solano, A.J., Lotsch, B.V.: Tracking molecular diffusion in one-dimensional photonic crystals. Adv. Mater. **30**(51), 1803730 (2018)
Vardeny, Z.V., Nahata, A., Agrawal, A.: Optics of photonic quasicrystals. Nat. Photonics **7**, 177–187 (2013)
Vyunishev, A.M., Pankin, P.S., Svyakhovskiy, S.E., Timofeev, I.V., Vetrov, S.Y.: Quasiperiodic one-dimensional photonic crystals with adjustable multiple photonic bandgaps. Opt. Lett. **42**, 3602–3605 (2017)
Wang, X., Zhou, L., Zhao, T., Liu, X., Feng, S., Chen, X., Guo, H., Li, C., Wang, Y.: High-sensitivity quasi-periodic photonic crystal biosensor based on multiple defective modes. Appl. Opt. **58**, 2860–2866 (2019)
Wang, Y., Chen, S., Wen, P.P., Liu, S., Zhong, S.: Multichannel filter based on tunable Fibonacci quasi-periodic structure for one-dimensional magnetized ternary plasma photonic crystal. Optik **224**, 165393 (2020)
Wu, J., Gao, J.: Low temperature sensor based on one-dimensional photonic crystals with a dielectric-superconducting pair defect. Optik **126**, 5368–5371 (2015)
Wu, C., Liu, X., Feng, S., Chen, X., Li, C., Wang, Y.: High-sensitivity silicon-based photonic crystal refractive index biosensor based on defect-mode coupling. Optic. Commun. **427**, 409–417 (2018)
Yeh, P.: Optical Wave in Layered Media. Wiley, Hoboken, NJ, USA (1988)
Zhang, H.F., Liu, S.B., Kong, X.K., Bian, B.R., Dai, Y.: Omnidirectional photonic band gap enlarged by one-dimensional ternary unmagnetized plasma photonic crystals based on a new Fibonacci quasi-periodic structure. Phys. Plasmas **19**, 112102 (2012)
Zhuo, Y., Hu, H., Wang, Y., Marin, T., Lu, M.: Photonic crystal slab biosensors fabricated with helium ion lithography (HIL). Sens. Actuator. A: Phys. **297**, 111493 (2019)